The Influence of the Shear-Induced Pressure Gradient on Thunderstorm Motion

RICHARD ROTUNNO AND JOSEPH B. KLEMP

National Center for Atmospheric Research[1], Boulder, CO 80307

(Manuscript received 8 August 1981, in final form 3 November 1981)

ABSTRACT

In the present investigation we propose a simple theory to explain how a veering environmental wind shear vector can cause an initially symmetric updraft to grow preferentially to the right of the shear vector and acquire cyclonic rotation. The explanation offered is based on linear theory which predicts that interaction of the mean shear with the updraft produces favorable vertical pressure gradients along its right flank. To assess the validity of linear theory for large-amplitude updrafts, the three-dimensional, shallow, anelastic equations are numerically integrated using a simple parameterization for latent heating within a cloud and the linear and nonlinear forcing terms are separately analyzed. These results suggest that although the nonlinear effects strongly promote splitting of the updraft, the linear forcing remains the dominant factor in preferentially enhancing updraft growth on the right flank. We believe this differential forcing is a major contributor to the observed predominance of cyclonically rotating, right moving storms.

1. Introduction

Why do most Great Plains tornadoes spin cyclonically? It has been known for some time that tornadoes are embedded within a cyclonically rotating portion of a thunderstorm called the mesocyclone (Brooks, 1949; Fujita, 1960). Why, then, do most rotating thunderstorms contain mesocyclones rather than mesoanticyclones? Tornadic storm proximity soundings (Maddox, 1976) reveal a characteristic curvature of the wind hodograph. We argue herein that it is this curvature which is most likely responsible for the prevalence of mesocyclones (rather than mesoanticyclones) and propose a simple theory to explain the result.

Numerical experiments by Wilhelmson and Klemp (1978) demonstrate how cyclonic and anticyclonic severe storms may evolve in the presence of environmental wind shear. They consider a shear flow in which the shear vector does not change direction with height. Since there is no horizontal variation of the environmental shear flow, there is initially no vertical vorticity or divergence. Coriolis effects are neglected for these experiments. Convection is initiated by an axisymmetric thermal and a vortex pair develops in a horizontal plane due to the upward tilting of the vortex tubes associated with the mean shear flow. Facing in the direction of the shear vector, there is positive vertical vorticity on the right side of the updraft and negative on the left. After a time, rain forms on the center axis of the original cell and is primarily responsible for inducing a downdraft which splits the original cell into two cells—one, dominated by cyclonic vorticity (at low levels), propagating to the right of the shear vector, the other dominated by anticyclonic vorticity, propagating to the left. The two storms possess mirror-image symmetry and resemble Browning's (1964, 1968) observationally-deduced model for severe right- and left-moving storms (denoted by SR and SL, respectively).

One might guess that the SR-type storm is more commonly observed in the Northern Hemisphere because of the cyclonic bias introduced by the earth's rotation. However, Klemp and Wilhelmson (1978b) found the inclusion of the Coriolis effect to only weakly enhance the SR storm over the SL in their model. Climatological data concerning wind hodographs associated with severe tornadic thunderstorms (the great majority of which are SR types) reveal a strong clockwise turning of the wind shear vector (in addition to the wind vector) between the surface and 700 mb (see Maddox, 1976). Klemp and Wilhelmson demonstrated that the relative strengths of the SR and SL storms were sensitive to the variation of the direction of the wind shear vector with height. Specifically, a *clockwise turning of the wind shear vector with height favors the development of a cyclonic, right-moving storm (even with no Coriolis effect) while conversely, a counterclockwise turning favors the anticyclonic, left-moving storm.*

To illustrate the preceding remarks, we present results of two numerical experiments from the cloud model developed by Klemp and Wilhelmson (1978a).

[1] The National Center for Atmospheric Research is sponsored by the National Science Foundation.

0027-0644/82/020136-16$08.00

Klemp *et al.* (1981) conducted numerical experiments with the goal of simulating the tornadic storm which occurred on 20 May 1977 near Del City, Oklahoma. The environmental hodograph used is displayed in Fig. 1. This hodograph indicates that the wind shear vector veers with height over the entire troposphere. [On a wind hodograph where V *vs* U is plotted, the direction of the wind shear vector $\partial \mathbf{V}/\partial z$ is obtained by considering the local tangent to the curve $V(U)$ and identifying the ordinate as northward and the abscissa as eastward.] The thermodynamic sounding and other details may be found in that paper. We present here two comparative experiments with the Coriolis effect neglected (the study of Klemp *et al.* included it). In addition to the 20 May sounding in Fig. 1, a straight line hodograph is included which contains approximately the same magnitude of wind shear below 6 km (with no shear above this height) but shows no variation of direction with height. Fig. 2a contains horizontal cross sections at 2.25 km above the surface of vertical velocity and rainwater fields at four stages of development for the straight line hodograph. During the early stage (20 min), the updraft is nearly axisymmetric, later (40 min) the updraft is elongated in the direction of the shear vector. By 60 min, rain formation on the central axis of the original cell splits the updraft into two updraft/downdraft pairs which thereafter (80 min) travel to the right and left of the shear vector, respectively. The vorticity fields (not shown) indicate that the right moving updraft is cyclonic and the left moving updraft is anticyclonic. We compare this development to the one which occurs using the 20 May hodograph in Fig. 2b. Notice that at 20 min the updraft becomes biased toward the right of the shear vector. At 40 min the right side of the splitting

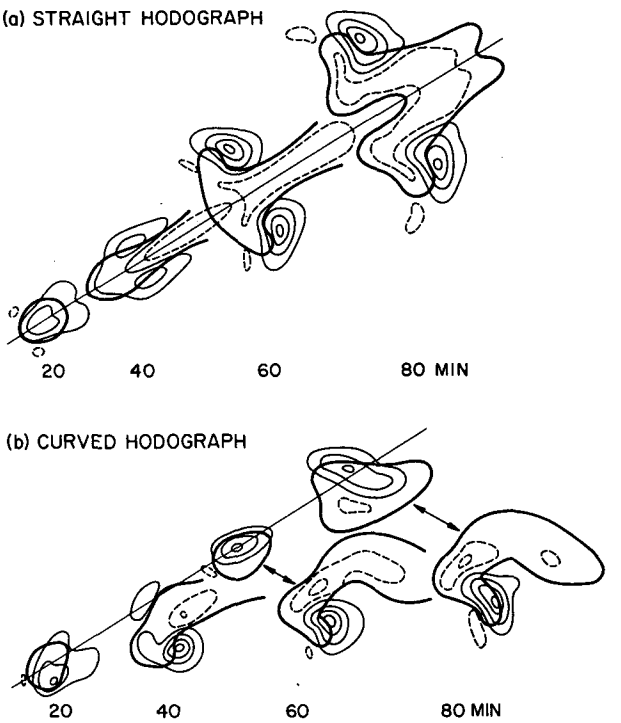

FIG. 2. Horizontal contour plots of vertical velocity at 2.25 km AGL at t = 20, 40, 60 and 80 min from the three-dimensional numerical cloud model developed by Klemp and Wilhelmson (1978a) for (a) the straight line hodograph of Fig. 1 and (b) the 20 May sounding also contained in Fig. 1. Updrafts (solid lines) and downdrafts (dashed lines) are contoured at 4 m s^{-1} increments, beginning at ±2 m s^{-1}. The heavy line is the outline of the 0.5 g kg^{-1} rainwater field predicted by the model. Note that in (a) the development is completely symmetric with respect to the diagonal line which represents the direction of the shear vector. The diagonal line in (b) is the same as in (a) and also corresponds to the direction of the shear vector at 2.25 km. Here the development is skewed so that the right member is enhanced over the left.

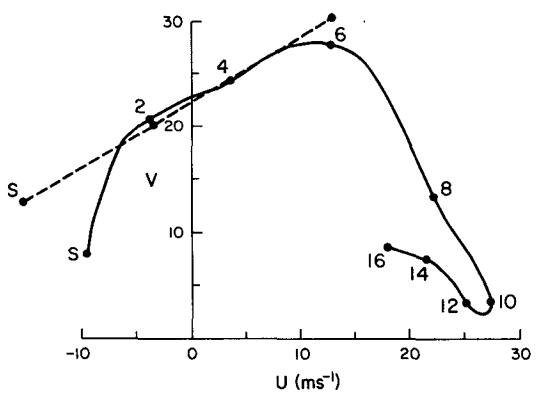

FIG. 1. Wind hodograph for severe thunderstorms which occurred near Del City, Oklahoma on 20 May 1977 with height labeled in kilometers. Curvature of the hodograph indicates veering of the wind shear vector with height. The straight line hodograph (dashed line) contains approximately the same magnitude of shear below 6 km, but does not vary the direction of the wind shear vector with height.

updraft is much stronger than the left, and at 60–80 min the right side ultimately dominates. Since Coriolis effects are neglected, the only possible reason for this bias is the curvature of the hodograph. A further refinement to this result is that hodograph curvature over the lowermost portion of the atmosphere is most important in producing the rightward bias. A hybrid case was simulated using the 20 May winds up to 4 km and the straight line hodograph above that point. This case developed similarly to that shown in Fig. 2b although the cyclonic storm deviated somewhat more slowly to the right. This influence of directional wind shear appears to be a general result and not peculiar to this numerical model; it occurs in all published numerical simulations where the environmental shear vector turns clockwise from the surface to mid-levels (cf. Schlesinger, 1978).

Impressed with the fact that the rightward bias occurs early in the numerical experiments, we felt

that if we could understand this initial bias, we would be a long way toward an explanation of why the turning shear vector favors the development of one member of the split pair. The initial amplitude of the convection in the cloud model is, by definition, small and linear theory is thus applicable. We've found that the simple relation which exists in the linear theory between the non-hydrostatic pressure and the wind shear vector can explain the early bias described above. *Specifically, the linear theory predicts that an initially axisymmetric updraft interacts with a shear flow in a way that produces a favorable (unfavorable) vertical pressure gradient, below the level of maximum vertical velocity, on the right (left) side of the updraft when the shear vector turns clockwise with height. Furthermore, the linear theory predicts the production (through the upward tilting of mean vortex tubes) of cyclonic vorticity on this right side to which the updraft is biased.* In a similar fashion the left side would be favored if the shear vector turned counterclockwise with height. [This explanation is reminiscent of, but distinctly different from, that of Newton (1960) who hypothesized that the clockwise turning of the wind produces the rightward bias.]

The linear theory as such is theoretically limited to small-amplitude motions. To evaluate the relevance of the linear theory and to gain knowledge concerning the role of nonlinear effects, we performed numerical integrations of simplified, three-dimensional equations of motion pertaining to buoyant convection in an environment where the wind shear vector may change direction with height. We analyze the contribution to the vertical acceleration from the pressure gradient associated with the linear, nonlinear and buoyancy terms and the vertical advection separately and find the linear effect is the only one which is responsible for the rightward bias described above. Further, we find that the pressure forcing due to the nonlinear dynamics can, through preferential uplift on the storm's flank, contribute to the storm splitting process.

The following section contains the governing equations and rationale for simplifications made. Consequences of the linear theory concerning the rightward bias are considered and the numerical integration of the nonlinear equation set is described. Results and analysis of these integrations are presented in Section 3. Further discussion and summary are included in Section 4.

2. Linear analysis and numerical model

As mentioned in the Introduction, we are impressed with the fact that when the shear vector changes direction with height an initially symmetric updraft at early times displays a systematic bias toward the flank which will subsequently become the stronger member of the split pair. At early stages in a thermal's development, the details of cloud microphysics are of minimal importance. Hence, for clarity of exposition, we have chosen a relatively simple convection model to study the way in which a turning wind shear vector acts to change the shape of an initially symmetric updraft. It is of course possible, and in fact likely, that initial convection in nature is not axisymmetric. However, it seems entirely unlikely that all initial convective elements are systematically biased in a way which favors the development of cyclonic, right-moving storms. The hypothesis of Klemp and Wilhelmson (1978b) is that a systematic bias can result through the interaction of an initially symmetric thermal with the shear flow. Klemp and Wilhelmson demonstrated that such a bias does occur in the numerical model; in the present study we develop a simple theory to explain why this is so.

In order to study the simplest set of equations which contains the relevant physics, we shall consider the shallow, inviscid anelastic equations (Ogura and Phillips, 1962)

$$\frac{\partial \mathbf{v}}{\partial t} + \mathbf{v}\cdot\nabla\mathbf{v} = -\nabla\pi + B\mathbf{k}, \tag{1}$$

$$\frac{\partial B}{\partial t} + \mathbf{v}\cdot\nabla B = -N^2 w, \tag{2}$$

$$\nabla\cdot\mathbf{v} = 0, \tag{3}$$

where $\mathbf{v}$, and B are the velocity vector and buoyancy respectively; $\pi \equiv c_p\theta_0(p/p_0)^{R/c_p}$, where p, p_0, R and c_p are the pressure, ground pressure, universal gas constant and the specific heat at constant pressure, respectively. The del operator is defined $\nabla \equiv \mathbf{i}\partial/\partial x + \mathbf{j}\partial/\partial y + \mathbf{k}\partial/\partial z$, where $\mathbf{i}$, $\mathbf{j}$, $\mathbf{k}$ are the unit vectors in the x, y and z directions, respectively. The Cartesian components of $\mathbf{v}$ are denoted by (u, v, w). $N \equiv [(g/\theta_0)(\partial\bar{\theta}/\partial z)]^{1/2}$ is the Brunt-Vaisala frequency, where g is the acceleration due to gravity and $B \equiv g\theta'/\theta_0$. The potential temperature $\theta \equiv \theta_0 + \bar{\theta}(z) + \theta'(\mathbf{x}, t)$, where θ_0 is a constant, $\mathbf{x}$ the position vector and t time. The initial conditions are

$$B(\mathbf{x}, 0) = B_0(\mathbf{x}), \tag{4a}$$

$$\mathbf{v}(\mathbf{x}, 0) = \mathbf{i}U(z) + \mathbf{j}V(z) + \mathbf{v}_0(\mathbf{x}), \tag{4b}$$

where $B_0(\mathbf{x})$ and $\mathbf{v}_0(\mathbf{x})$ are chosen to be axisymmetric with respect to the vertical axis. Our principal concern will be with determining the mechanism(s) by which the axisymmetric updraft (produced by the axisymmetric warm thermal) becomes asymmetric. To quantify the discussion, we consider the vertical component of Eq. (1)

$$\frac{\partial w}{\partial t} = -\mathbf{v}\cdot\nabla w - \frac{\partial \pi}{\partial z} + B. \tag{5}$$

Within this model, w may change locally by advec-

tion, vertical pressure gradients and buoyancy. Perhaps the most enigmatic of these three terms is the vertical pressure gradient. Estimation of the non-hydrostatic pressure gradient by way of obstacle flow analogies has dominated theoretical discussions of severe storms ever since Newton and Newton (1959) first suggested it. The obstacle flow analogy is appealing because it provides a relatively simple way of viewing a complex physical problem. However, such analogies are difficult to justify rigorously. For example, flow around circular cylinders in the laboratory has various configurations depending on the Reynolds number, whether or not separation occurs, etc. Furthermore, the flow around a cylinder in a stream flow which varies along the axis of the cylinder may be highly complex. Since there is no obstacle in the atmosphere, how does one decide *a priori* what aspect of cylinder flow is relevant? We shall make further comments on this analogy in Section 4c. One approach toward understanding the pressure gradient term is through direct calculation from three-dimensional numerical model calculations. Schlesinger (1980) has calculated the contributions to the pressure from hydrostatic, non-hydrostatic and drag sources for one numerical model case study. He found that the non-hydrostatic vertical pressure gradient contributes to updraft splitting by forcing positive vertical velocity on the flanks of the original cell (see his Fig. 9). That this forcing is greater on the right (south) flank is, we believe, a direct consequence of the fact that his hodograph exhibits a wind shear vector which turns clockwise with height. This effect is predicted by the linear theory we now develop.

a. Linear theory

We consider Eqs. (1)–(3) linearized about the environmental wind vector $\mathbf{V} = [U(z), V(z), 0]$:

$$\frac{D}{Dt}\mathbf{v}' + w'\frac{d}{dz}\mathbf{V} = -\nabla\pi' + B'\mathbf{k}, \tag{6}$$

$$\frac{D}{Dt}B' = -N^2 w', \tag{7}$$

$$\nabla\cdot\mathbf{v}' = 0, \tag{8}$$

where $D/Dt = \partial/\partial t + \mathbf{V}\cdot\nabla$. Because the mechanism we investigate is not directly related to buoyancy effects, we consider for the moment a homogeneous fluid ($B' = N^2 = 0$), flowing horizontally at a velocity $\mathbf{V}(z)$. Suppose at $t = 0$, we specify an axisymmetric updraft $w_0'(\mathbf{x})$ with perturbation horizontal components $u_0'(\mathbf{x})$, $v_0'(\mathbf{x})$ specified such that continuity [Eq. (8)] is satisfied.

Moving with the mean flow, the vertical velocity changes according to the vertical component of (6), that is

$$\frac{Dw'}{Dt} = -\frac{\partial\pi'}{\partial z}. \tag{9}$$

We obtain an equation for π' by taking the divergence of (6), i.e.,

$$\nabla^2\pi' = -2\frac{d\mathbf{V}}{dz}\cdot\nabla w'. \tag{10}$$

The qualitative behavior of the solution of (10) may be found by noting that for a function consisting of a narrow band of Fourier components, the Laplacian of the function is negatively proportional to the function itself. In this situation, Eq. (10) becomes

$$\pi' \sim \frac{d\mathbf{V}}{dz}\cdot\nabla w'. \tag{11}$$

Since the forcing functions we examine have small band width, we expect Eq. (11) to be approximately correct away from boundaries. Evaluation of this approximation in numerical simulations presented in Section 3b also confirms its qualitative validity.

We now consider the pressure field associated with the initial symmetric updraft $w_0'(\mathbf{x})$. Relation (11) indicates that high pressure will form on the upshear flank of the updraft with low pressure on the downshear flank. Thus, at any given height a negative horizontal pressure gradient forms across the updraft in the direction of the environmental wind shear vector. If the shear vector is independent of height, then the pressure varies with height in proportion to $\nabla w_0'$. A simple illustration will facilitate the ensuing discussion. Fig. 3a displays an initial impulse in a one directional shear flow $\mathbf{V}(z) = [U(z), 0, 0]$ where for simplicity we take $U = \alpha z$, $\alpha > 0$. Relation (11) becomes

$$\pi' \sim \alpha\frac{\partial w_0'}{\partial x}.$$

Referring to Fig. 3a, we observe that since $\partial U/\partial z > 0$, there is high pressure on the west (according to the standard meteorological convention) side of the updraft because $\partial w_0'/\partial x > 0$. Conversely there is low pressure on the east side. The high and low pressures have maximum amplitude at the height where w_0' (and consequently, $\partial w_0'/\partial x$) has its largest values. Hence, as indicated in the diagram, the pressure distribution tends to prevent the shearing apart of the updraft which would occur if only the advection term were operative. Further, this favorable non-hydrostatic pressure gradient may play a crucial role in lifting negatively buoyant sub-cloud air (e.g., as observed by Marwitz, 1972) to its level of free convection. Note that the direction of the high/low pressure pattern aligns with the shear vector on a symmetric updraft. If the shear vector does not change direction with height, the relative highs will be vertically stacked as will the lows and the flow develops symmetrically about the shear vector. We emphasize that a veering wind situation may not be fundamentally different from the case described above. That is, a wind hodograph may exhibit wind veering but no change in *direction* of the wind shear vector. Thus,

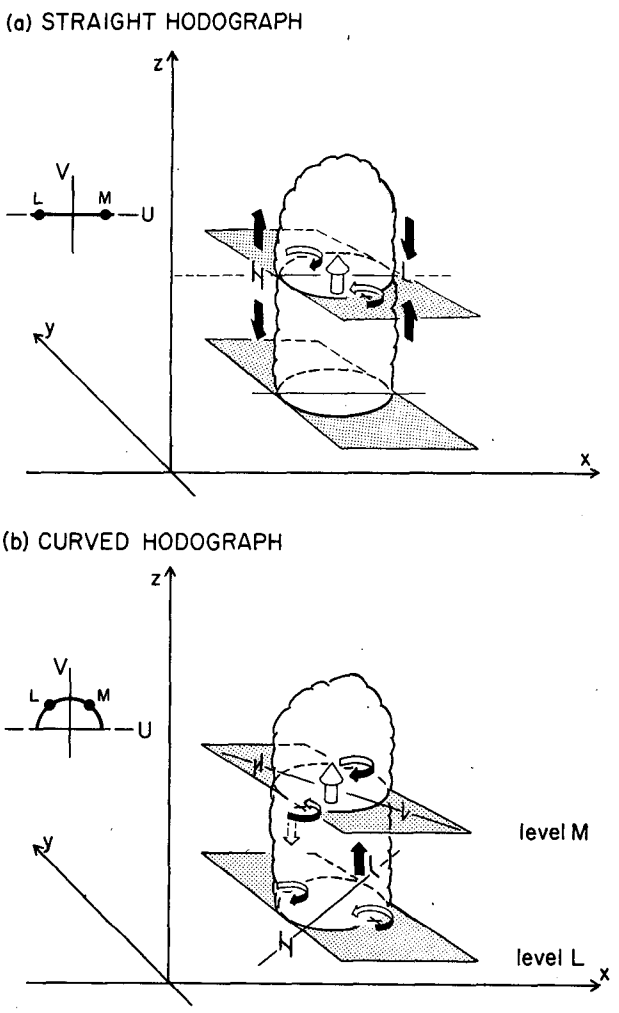

FIG. 3. Schematic which illustrates the behavior of pressure and vorticity as implied by Eqs. (11) and (12), respectively, for (a) a case where the wind shear vector does not change with height and (b) a case where the wind shear vector veers with height. The corresponding hodographs for environmental flow at low (L) to mid (M) levels are inset to the left. Horizontal pressure gradients parallel to the shear vector are labeled at each level along with the preferred locations of positive (+) and negative (−) vorticity. The orientations of the resulting vertical pressure gradient forces between low and mid levels are indicated by the black arrows.

any straight line hodograph produces the same behavior as described above.

When the shear vector changes direction with height, the situation is fundamentally different because now there is no axis of symmetry in the fluid. Fig. 3b contains a hypothetical hodograph in which a shear vector pointing toward the northeast at low levels turns toward the southeast at middle levels. The diagram in Fig. 3b illustrates that at low levels there is a high to the southwest and a low to the northeast, and at a higher level, the horizontal pressure gradient turns with the shear vector so that there is a high to the northwest and a low to the southeast. Thus, vertical pressure gradients are created which assist rising air on the southern side of the updraft and inhibit upward motion on the northern side. It is in this fashion, we believe, that an initially symmetric updraft becomes biased toward the right side.

The tendency of the rightward moving storm to have stronger vorticity than its leftward moving counterpart given a veering wind shear vector was also noted by Klemp and Wilhelmson (1978b). Here we consider the vertical component of the curl of (6), i.e.,

$$\frac{D}{Dt}\zeta' = \mathbf{k}\cdot\left(\frac{d\mathbf{V}}{dz}\times\nabla w'\right), \tag{12}$$

where $\zeta' \equiv \partial v'/\partial x - \partial u'/\partial y$ is the vertical component of the perturbation vorticity vector $\omega' \equiv (\xi', \eta', \zeta')$. The right-hand side of (12) represents the linearized version of vortex-line tilting. Notice the contrasting forms of the vorticity production term in Eq. (12) and the pressure perturbation Eq. (11). While pressure perturbations are aligned parallel to the shear vector, vertical vorticity perturbations are oriented perpendicular to the shear vector. The environmental vorticity associated with the mean shear is

$$\nabla\times\mathbf{V}(z) = \mathbf{k}\times\frac{d\mathbf{V}}{dz}.$$

Hence, these horizontal vortex lines at any level z are oriented perpendicular to the shear vector. According to (12), cyclonic (positive) vorticity is produced on the right (facing in the direction of the shear vector) and anticyclonic is produced on the left of a symmetric updraft. When the shear vector direction does not vary with height, the positive vorticity maxima are vertically stacked to the right of the shear vector as are the negative minima on the left. Because of the assumed symmetry of w, the magnitudes of the positive and negative vorticity extrema are identical. The schematic diagram in Fig. 3a illustrates where positive and negative vertical vorticity are produced by tilting.

When the shear vector turns with height, the orientation of the vortex pair turns with the shear vector in accordance with the right hand side of (12). As illustrated in Fig. 3b, *the production of positive vorticity is on the side where favorable pressure gradients have been created due to the turning shear vector*, i.e., cyclonic vorticity and updraft production are positively correlated.

To prove this result more generally, consider the flow in the cylindrical coordinates (r, ϕ, z). Thus

$$\nabla w' = \frac{\partial w'}{\partial r}\mathbf{e}_r + \frac{1}{r}\frac{\partial w'}{\partial \phi}\mathbf{e}_\phi + \frac{\partial w'}{\partial z}\mathbf{e}_z,$$

where $\mathbf{e}_r$, $\mathbf{e}_\phi$ and $\mathbf{e}_z$ are the unit vectors; for an axisymmetric updraft the second term is zero. The mean wind vector in this coordinate system is

$$\mathbf{V}(z) = (U\cos\phi + V\sin\phi)\mathbf{e}_r - (U\sin\phi - V\cos\phi)\mathbf{e}_\phi.$$

To relate our results to hodograph features we let $V = V(U)$ and thus $\partial V/\partial z = (\partial V/\partial U)\partial U/\partial z$ for $\partial U/\partial z \neq 0$. Using this definition of V and (11), Eqs. (9) and (12) become

$$\frac{Dw'}{Dt} \sim -\frac{\partial}{\partial z}\left[\left(\cos\phi + \frac{\partial V}{\partial U}\sin\phi\right)\frac{\partial w'}{\partial r}\frac{\partial U}{\partial z}\right],$$

$$\frac{D\zeta'}{Dt} \sim \left(\sin\phi - \frac{\partial V}{\partial U}\cos\phi\right)\frac{\partial w'}{\partial r}\frac{\partial U}{\partial z},$$

respectively.

It is easy to show with these relations that for any location (r, z),

$$\int_0^{2\pi} \frac{Dw'}{Dt}\frac{D\zeta'}{Dt}\,d\phi \sim -\frac{\partial^2 V}{\partial U^2}\left(\frac{\partial U}{\partial z}\right)^3\left(\frac{\partial w'}{\partial r}\right)^2. \quad (13)$$

Thus, there is a positive correlation between updraft and vorticity production when the hodograph curvature ($\partial^2 V/\partial U^2$) is negative (for $\partial U/\partial z > 0$, which is the typical case) which corresponds to veering of the wind shear vector. This correlation can increase the magnitude of the positive vorticity maxima over the magnitude of the negative vorticity minima through processes which will be examined in Section 4b.

To evaluate the specific predictions of the linear theory, we display in Fig. 4, p, ζ and w from the three-dimensional cloud model experiment described in Fig. 2b. Fig. 4a contains horizontal contour plots of the vertical vorticity, pressure and vertical velocity at z = 1.0 km at t = 15 min. The shear vector at z = 1.0 km is from 198°. The vorticity pattern produced through vortex tilting is approximately aligned perpendicular to the shear vector with positive vorticity on the right and negative on the left. There is a relative pressure maximum upshear and a pressure minimum downshear. The updraft maximum is biased to the right of the shear vector, toward the positive vorticity maximum which is greater in magnitude than the negative minimum. At 5.0 km (Fig. 4b), the shear vector is from 246° and the vorticity and pressure patterns again align with the shear vector at that level. The high/low pressure pattern veers from an essentially north/south orientation at low levels to an east/west orientation at higher levels. Thus, there are favorable vertical pressure gradients on the south and east sides with the most favorable gradient probably in between on the southeast flank where we witness the updraft to grow preferentially.

As illustrated in Fig. 2, storm splitting and the development of right and left moving storms can occur with or without hodograph curvature. However, we believe the preceding arguments demonstrate that the bias of the right-moving cyclonic storm over the left-moving anticyclonic storm is a direct consequence of the veering shear vector and

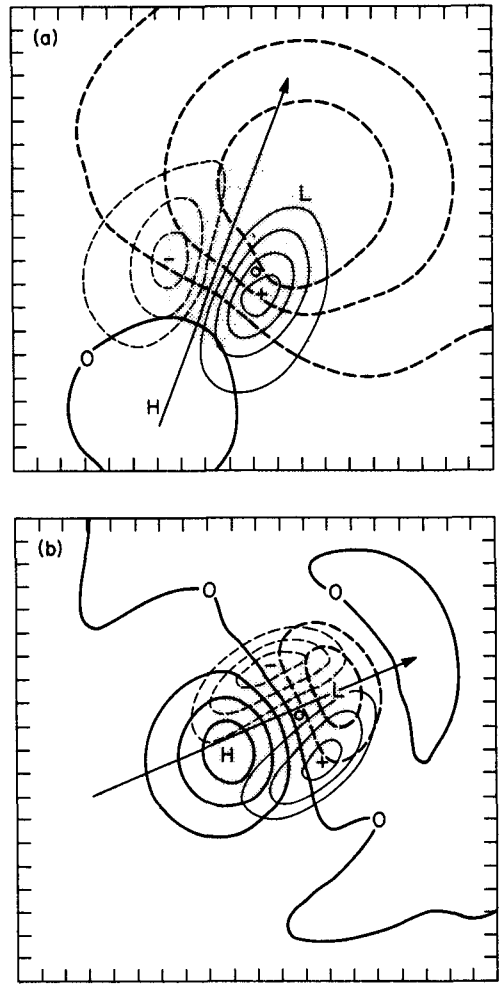

FIG. 4. Horizontal contour plots of vertical vorticity (thin lines, 10^{-3} m s^{-1} contour interval), pressure (heavy lines, 0.2 mb contour interval) and vertical velocity (updraft shaded with o at maximum) from the three-dimensional cloud simulation of Fig. 2b at t = 15 min at (a) z = 1.0 km and (b) z = 5.0 km. The long arrow represents the direction of the environmental shear vector at that level. Note that the pressure and vorticity patterns align nearly parallel and perpendicular to the shear vector as predicted by Eqs. (11) and (12), respectively.

is a linear effect. To justify this conclusion we shall next consider the role of buoyancy and nonlinear effects through numerical solution of Eqs. (1)–(3) described in the following subsection.

b. *Numerical integration and analysis*

In the numerical model calculations, Eqs. (1)–(3) are approximated by a set of finite-difference equations on a staggered grid. Derivatives are second-order accurate and the leap-frog method is used for time integration. The diagnostic pressure equation is obtained by taking the divergence of (1) and using

(3) which yields

$$-\nabla^2\pi = \left(\frac{\partial u}{\partial x}\right)^2 + \left(\frac{\partial v}{\partial y}\right)^2 + \left(\frac{\partial w}{\partial z}\right)^2 + 2\frac{\partial u}{\partial y}\frac{\partial v}{\partial x} + 2\frac{\partial u}{\partial z}\frac{\partial w}{\partial x} + 2\frac{\partial v}{\partial z}\frac{\partial w}{\partial y} - \frac{\partial B}{\partial z}, \quad (14)$$

and is solved every time step. The domain is bounded above and below by rigid parallel plates where $w = 0$; since the early development of convection is of primary interest, periodic lateral boundary conditions are specified for simplicity without adversely affecting the results. The initial conditions are given by (4) and will be specified below. Eqs. (1)–(3) are inviscid and thus no mixing terms are included in the model. Tests with the full cloud model indicate that this is a good approximation during the early development of convection. In simulating moist convection, a device which we've found useful for qualitatively replicating results obtained in the full three-dimensional cloud model is to let $N^2 = -N_w^2$ for $w > 0$ and $N^2 = N_d^2$ for $w < 0$, where $N_w^2 = 5 \cdot 10^{-6}$ s^{-2} and $N_d^2 = 5 \times 10^{-5}$ s^{-2}. This is intended to simulate latent heating in the updraft and adiabatic warming in the return flow and is similar to the conditional instability model used by Lilly (1960).

We are concerned with the mechanisms by which a storm updraft propagates and how it may change shape as it moves. Eq. (5) contains the desired information but in too compact a form to be easily digested. To provide a more meaningful analysis, we shall consider the contributions to π from three effects: linear, nonlinear and buoyancy, that is,

$$\pi = \pi_L + \pi_{NL} + \pi_B . \quad (15)$$

Details of this analysis are included in the Appendix. The model domain is 10 km deep and is 32 km $\times$ 32 km in the horizontal. The vertical grid size $\Delta z = 500$ m and the horizontal grid size $\Delta x = \Delta y = 1$ km. The time step $\Delta t = 20$ s.

The effect of buoyancy on vertical acceleration is contained in the expressions $-\partial\pi_B/\partial z + B$ and is referred to as the buoyancy forcing. The contributions to the negative vertical pressure gradient from the linear and nonlinear terms in the momentum equation are $-\partial\pi_L/\partial z$ and $-\partial\pi_{NL}/\partial z$, respectively. The advection of vertical velocity is also computed. The four terms together with their sum $\partial w/\partial t$ are discussed in the following section.

3. Results

The initial conditions are specified according to (4a) and (4b) with $v_0(\mathbf{x}) = 0$ and the initial thermal disturbance is given by

$$B_0(\mathbf{x}) = \begin{cases} \Delta B \cos^2\frac{\pi}{2}X, & X \equiv \left[\left(\frac{x}{x_0}\right)^2 + \left(\frac{y}{y_0}\right)^2 + \left(\frac{z}{z_0} - 1\right)^2\right]^{1/2}, \quad X < 1 \\ 0, & \text{(otherwise)} \end{cases} \quad (16)$$

where $\Delta B = 0.1$ m s^{-2}, $x_0 = y_0 = 10$ km, $z_0 = 1.4$ km, and the center of the domain is at $x = y = 0$. The scale of this initial perturbation is chosen to be similar to that used in the full cloud model simulations. However, the same qualitative evolution occurs if the initial scale is specified to be smaller or larger.

a. Straight line hodograph

We first consider the response of the fluid to the thermal impulse (16) when the environmental wind-shear vector does not change direction with height. The wind profile we use is

$$U(z) = \begin{cases} 30\left(\frac{z}{z_s}\right) - 12 \text{ m s}^{-1}, & 0 \leq z \leq z_s \\ 18 \text{ m s}^{-1}, & z_s \leq z \leq 10 \text{ km} \end{cases}, \qquad V(z) = 0, \quad 0 \leq z \leq 10 \text{ km} \quad (17)$$

where $z_s = 4$ km is the depth of the shear layer. The hodograph is displayed in Fig. 5. Fig. 6a contains horizontal contour plots of w at $z = 1.5$ km at $t = 5$, 10 and 15 min. The axisymmetric thermal initially produces a symmetric vertical motion field. The updraft continues to grow and elongates in the direction of the shear vector ($t = 10$ min) and by 15 min the updraft is splitting. The integration was terminated at this time because the neglect of more detailed cloud physics and turbulence processes begins to corrupt the realism of the simulations. Thus, the integrations are carried out long enough for the nonlinear terms to become significant (because $w_{max} \approx 10$ m s^{-1}), yet short enough so that we may neglect rain formation, turbulence, etc.

Figs. 7a–7f display horizontal cross-sections of the forcing terms in the vertical momentum equation as described above. They correspond to the vertical motion field at $t = 10$ min, $z = 1.5$ km shown in Fig. 6a. At this time the maximum vertical velocity is approximately 11 m s^{-1} at $z = 3.5$ km. Hence, the forcing terms are displayed at a level approximately halfway between the ground and the level of w_{max}. The vertical pressure gradient associated with the linear terms in the momentum equation (hereafter referred to for brevity as the linear shear forcing)

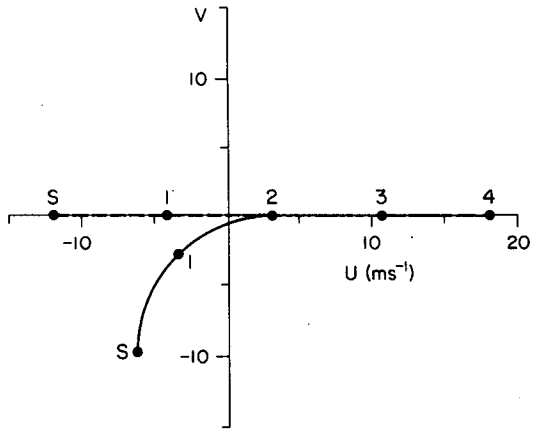

FIG. 5. Two idealized hodographs which represent a case where the wind shear vector does not vary with height (dashed line below 2 km, solid line above 2 km) and one where the wind shear vector veers with height (solid line). Heights above ground are labeled in kilometers.

indicates (Fig. 7a) uplift on the east (downshear) side and a downward force on the west side of the updraft. This behavior is consistent with relation (11) and the schematic diagram in Fig. 3a. The buoyancy pressure forcing (Fig. 7b) is basically symmetric with somewhat weaker values on the axis and displaced slightly upshear. The pressure gradient associated with the nonlinear terms in the momentum equation (Fig. 7c) is striking in that it induces strong uplift on both the left and right flanks. The advection of vertical velocity (Fig. 7e) acts to decrease w; at earlier times, the pattern is essentially opposite in sign to the linear shear forcing (Fig. 7a) as one would expect from calculating $-\mathbf{V}(z)\cdot\nabla w'$, while at $t = 10$ min the vertical advection $-ww_z$ is important and negative at this level. The sum of all these terms is the local rate of change of w, $\partial w/\partial t$, and is displayed in Fig. 7f. Recalling the split structure of the vertical motion field at $t = 15$ min, it is clear that the nonlinear terms are the most important in producing this splitting.

To gain another perspective, we display w together with the linear shear, buoyancy and nonlinear forcings in vertical cross sections through w_{max} both along (x–z sections) and across (y–z sections) the shear at $t = 10$ min in Fig. 8. The updraft in the x–z section is basically erect and appears to resist the shear, which would tend to advect the updraft to the left at low levels and to the right at upper levels. Note the symmetry of w in the y–z section. The linear shear forcing along and across the shear is displayed in Fig. 8b. This forcing along the shear behaves as predicted by Eq. (11) and illustrated in Fig. 3a; below the level of w_{max} there is uplift downshear and a downward force on the upshear side. Above the level of w_{max} the converse is true, and hence this effect counters the distortion effect of differential horizontal advection. The linear forcing across the shear is negligible, which is consistent with Eq. (11). The buoyancy forcing (Fig. 8c) is essentially in phase with the vertical velocity structure as one might expect given the simple parameterization of the conditional instability. The nonlinear forcing (Fig. 8d) along the shear exhibits positive forcing below w_{max} on both the upshear and downshear sides with the latter approximately four times larger than the former. The nonlinear forcing is negative above w_{max}. Across the shear, the nonlinear forcing indicates the same behavior but is symmetric about the shear vector; the positive maxima on the left and right flanks again are believed to be the primary mechanism for producing the split updraft at $t = 15$ min (Fig. 6a) in this simple model. More will be said concerning the physics of this term in Section 4a.

b. *Curved hodograph*

We now perform the same analysis for a case where the wind shear vector veers with height, *viz.*

$$U(z) = \begin{cases} \dfrac{-30}{\pi}\cos\pi\left(\dfrac{z}{z_s}\right) + 3\ \text{m s}^{-1}, & 0 \leqslant z \leqslant 2\ \text{km} \\ 30\left(\dfrac{z}{z_s}\right) - 12\ \text{m s}^{-1}, & 2 \leqslant z \leqslant z_s \\ 18\ \text{m s}^{-1}, & z_s \leqslant z \leqslant 10\ \text{km} \end{cases}$$

$$V(z) = \begin{cases} \dfrac{30}{\pi}\left\{\sin\pi\dfrac{z}{z_s} - 1\right\}\text{m s}^{-1}, & 0 \leqslant z \leqslant 2\ \text{km} \\ 0, & 2 \leqslant z \leqslant 10\ \text{km} \end{cases} \qquad (18)$$

where again $z_s = 4$ km. The corresponding hodograph is displayed in Fig. 5. The wind profile is specified such that the hodograph curvature is confined between the ground and 2 km. Above 2 km, the hodograph is identical to the straight line case exam-

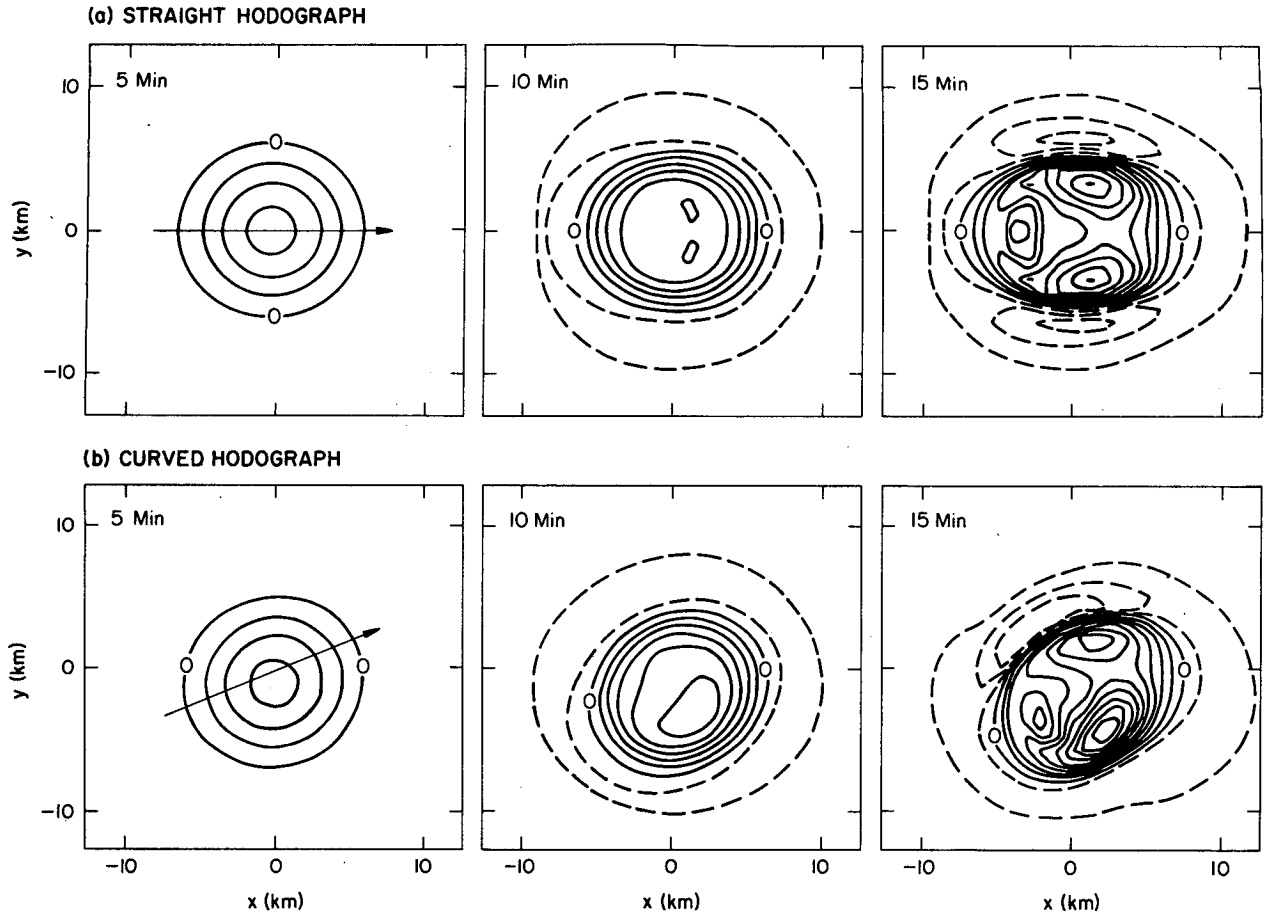

FIG. 6. Horizontal contour plots of w at z = 1.5 km at t = 5, 10 and 15 min from the numerical convection model described in Section 3b for (a) the straight line hodograph and (b) the curved line hodograph of Fig. 5. The vertical velocities are contoured at 2 m s^{-1} intervals. The long arrow in the plots at 5 min indicates the direction of the environmental wind shear vector at z = 1.5 km.

ined above. In addition, the magnitude of the shear, $\{(\partial U/\partial z)^2 + (\partial V/\partial z)^2\}^{1/2}$, is constant over the lowermost 4 km and equal to the value in the straight hodograph case.

Fig. 6b exhibits horizontal contour plots of w at z = 1.5 km at t = 5, 10 and 15 min. Again, the updraft is nearly symmetric during the first 5 min. However, by 10 min there is a marked bias of the updraft toward the right of the shear vector. At 15 min, the updraft splits as it does in the straight line case, although the right member of the pair is now stronger. Figs. 9a–9f display the forcing terms for the curved hodograph similarly to those in Figs. 7a–7f for the straight line hodograph. Not only does the linear shear forcing conform to the linear prediction of (11) and bias the updraft to the right, but cursory examination of the other forcing terms indicates the linear forcing is the only one contributing to such a bias. That is, the buoyancy, nonlinear and advection forcings are much as they were in the straight hodograph case, being, in fact, slightly biased to the left; this leaves only the linear shear effect described in Section 2a to account for the rightward bias.

4. Summary and discussion

The calculations presented herein are limited to what we hypothesize to be the initial stages of cumulus convection in a general wind shear. We've demonstrated that linear theory predicts the rightward bias of an initially axisymmetric thermal and using a simplified three-dimensional convection model, shown that the linear effect is the only one responsible for the early rightward bias. However, certain aspects of the nonlinear forcing display features which merit further discussion.

a. The role of the nonlinear effects vis-à-vis storm splitting

Schlesinger (1980) documented that non-hydrostatic pressure gradients produce preferential uplift

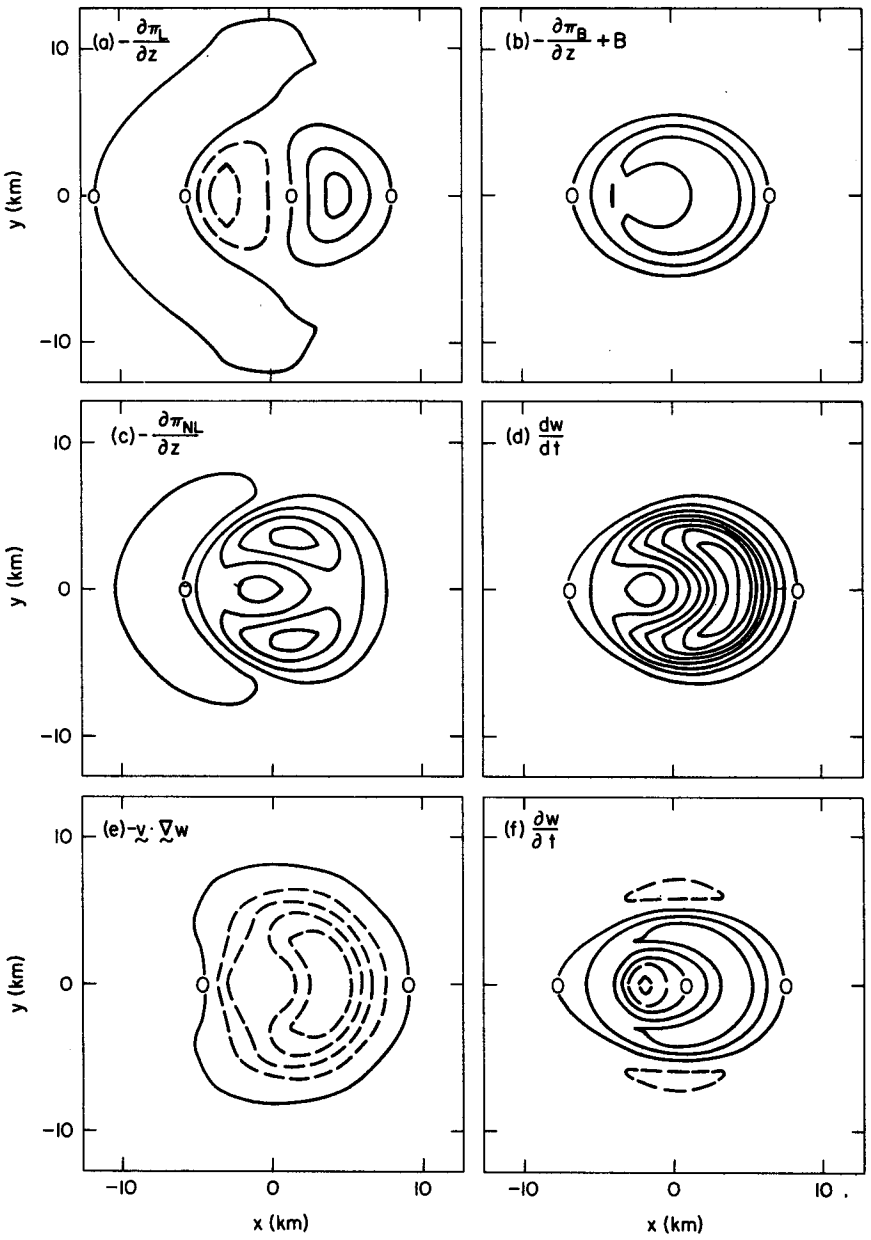

FIG. 7. Horizontal contour plots at $z = 1.5$ km, $t = 10$ min for the straight line hodograph case of (a) the linear pressure forcing, $-\partial\pi_L/\partial z$; (b) the buoyancy pressure forcing, $-\partial\pi_B/\partial z + B$; (c) the nonlinear pressure forcing, $-\partial\pi_{NL}/\partial z$; (d) dw/dt which is the sum of (a), (b) and (c); (e) the advection of w, $-\mathbf{v}\cdot\nabla w$; and (f) $\partial w/\partial t$ which is the sum of (d) and (e). The contour interval is 0.004 m s^{-2}.

on the flanks of the original updraft cell which contribute to updraft splitting. Fig. 7c and Fig. 8d (across shear) illustrate that the vertical pressure gradients which promote splitting are, in fact, associated with the nonlinear dynamic terms in the momentum equations. (Recall that the non-hydrostatic pressure gradient as illustrated in Fig. 7d has been divided into the three contributions shown in Figs. 7a, 7b and 7c.) Of the six nonlinear terms on the righthand side of Eq. (14), notice that three are related to fluid extension while the other three involve fluid shear. We first consider the fluid shear term $2u_y v_x$. Since

$$4u_y v_x = \{\text{horizontal shearing deformation}\}^2 - \{\text{vertical vorticity}\}^2,$$

a wind field in pure rotation has $2u_y v_x = -\frac{1}{2}\zeta^2$. Re-

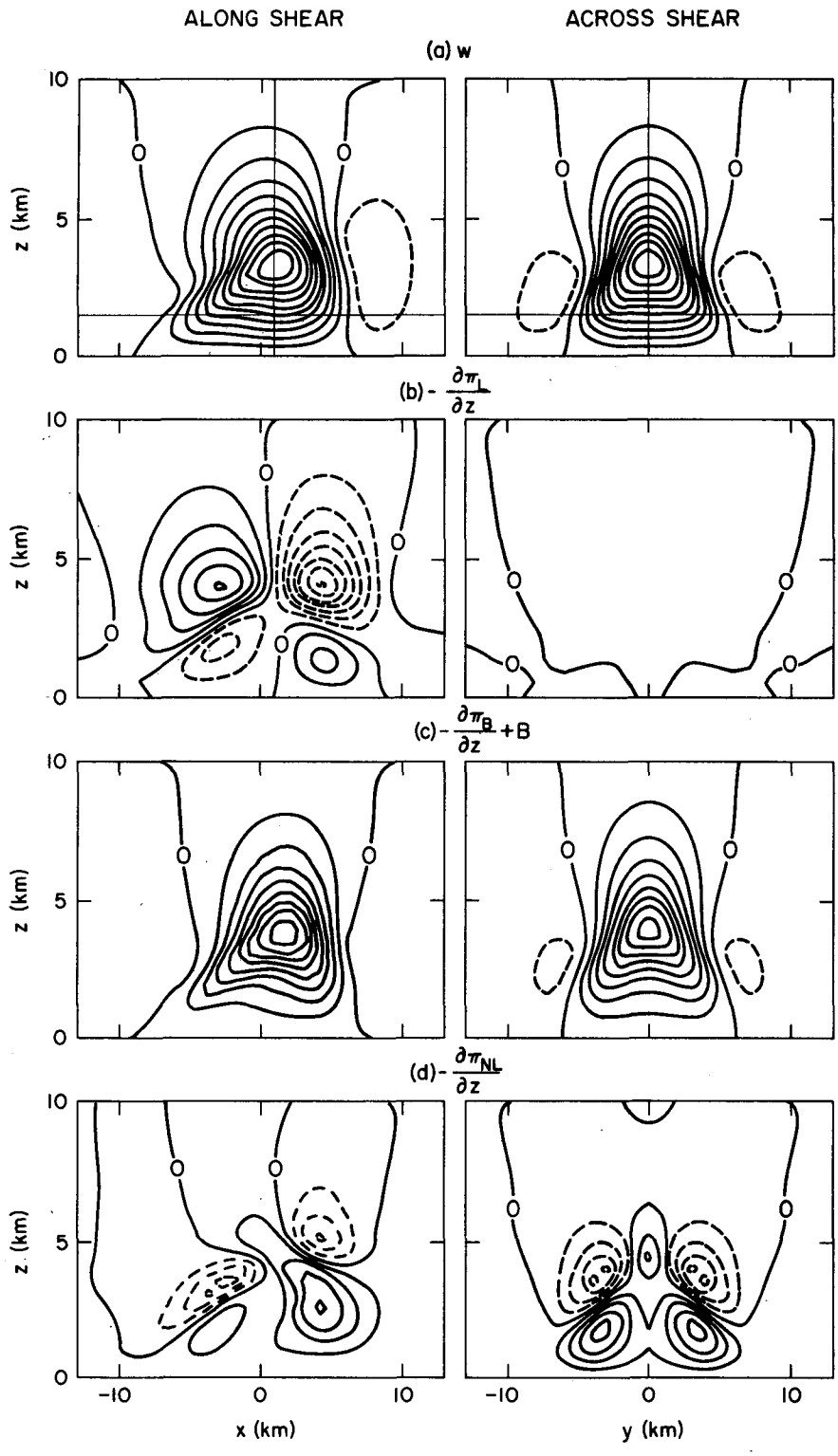

FIG. 8. Vertical contour plots along (x–z sections) and across (y–z sections) the shear at t = 10 min for the straight line hodograph case of (a) w, contoured every 2 m s^{-1}, (b) the linear forcing, (c) the buoyancy forcing and (d) the nonlinear forcing. Vertical velocity is contoured in 1 m s^{-1} intervals while the last forcing is contoured every 0.004 m s^{-2}.

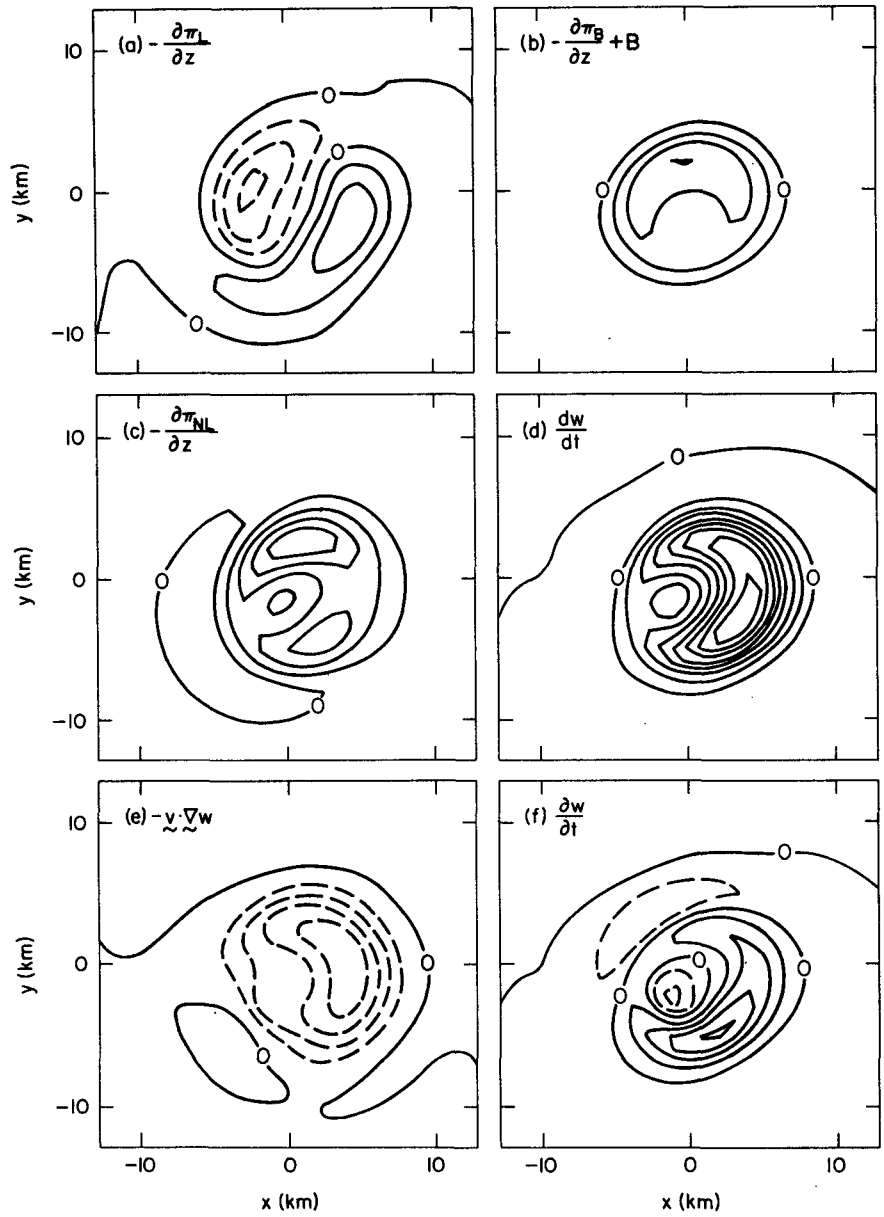

FIG. 9. As in Fig. 7 except for the curved hodograph displayed in Fig. 5.

calling (11) and (14), the perturbation pressure is then related to the vertical vorticity according to

$$\pi' \sim -\zeta^2. \tag{19}$$

Thus, the pressure is lower where the magnitude of the vorticity is higher. [This is a familiar result from large-scale meteorology. The geostrophic relation between pressure and vorticity is $\nabla_H^2 \pi' = -f\zeta_G$, and, using the same approximation which leads to (11), we obtain $\pi' \sim -f\zeta_G$. That is, the pressure is lower where the relative vorticity is higher. This geostrophic relation is obtained from (19) by setting $\zeta = f + \zeta_G$, neglecting the square of ζ_G and absorbing $-f^2$ into the definition of pressure.]

Before attempting to use Eq. (19) for diagnosis, some notes of caution are in order. For pure shearing deformation, $u_y v_x \neq 0$ and yet $\zeta = 0$ (Prandtl and Tietjens, 1934, p. 82). Also, in a two-dimensional [e.g., $\partial/\partial x = 0$, $u = u(y, z)$] flow, $u_y v_x = 0$ but $\zeta = -u_y \neq 0$. However, in the numerically modeled storm (Fig. 4), the type of vortex motion occurring on the updraft flanks displays a vortex pair and the vorticity is localized rather than two-dimensional; hence, where there is vorticity, it is related to the pressure approximately by expression (19). This re-

sult suggests that low pressure is induced by rotation on the updraft flanks which promotes lifting and this contributes to the splitting process.

The two remaining nonlinear fiuid shear terms, $2u_z w_x$ and $2v_z w_y$, are similar to $2u_y v_x$ and may be related to the x and y components of the vorticity vector, respectively, in the same manner as $2u_y v_x$ was related to ζ. These terms also tend to be maximized near the level of maximum ∇w, but unlike $2u_y v_x$, do not vanish on the symmetry axis along the shear vector. This is because a large contribution to the horizontal vorticity is from horizontal gradients of buoyancy which tend to act symmetrically (although distorted by the mean shear) about the updraft center producing a horizontal vortex ring around the periphery of the updraft. Further numerical computations (not presented) suggest that these two terms may have an influence on splitting which is comparable to the $u_y v_x$ term.

The first three terms on the right hand side of Eq. (14) which we've identified with fluid extension are unlikely contributors to the splitting tendency. To illustrate the influences of these terms consider a simple axisymmetric updraft of the form

$$w = h(r) \sin \frac{\pi z}{H},$$

where $r = (x^2 + y^2)^{1/2}$ and $h(0) = h_{\max}$ and $|h(r)| \to 0$ as $r \to \infty$. Evaluating these three extension terms and again following the same procedure which leads to approximate relation (11) yields

$$\pi' \approx f'(r) \cos^2 \frac{\pi z}{H},$$

where $f'(r)$ is a functional of h which is also maximized at $r = 0$. Thus, the pressure perturbation associated with this effect is zero at the level of $w_{\max}$ and positive above and below. For the structure of $h(r)$ described above, the effect is maximized on the central axis of w.

Hence, we speculate that with regard to the preferential forcing on the left and right flanks, the shear terms have the highest efficacy.

b. Selective enhancement of the positive vorticity when the shear vector veers

We've shown that when the environmental shear vector veers with height, an initially symmetric updraft becomes biased toward the right of the shear vector, where positive vorticity is produced by the upward tilting of vortex tubes associated with the

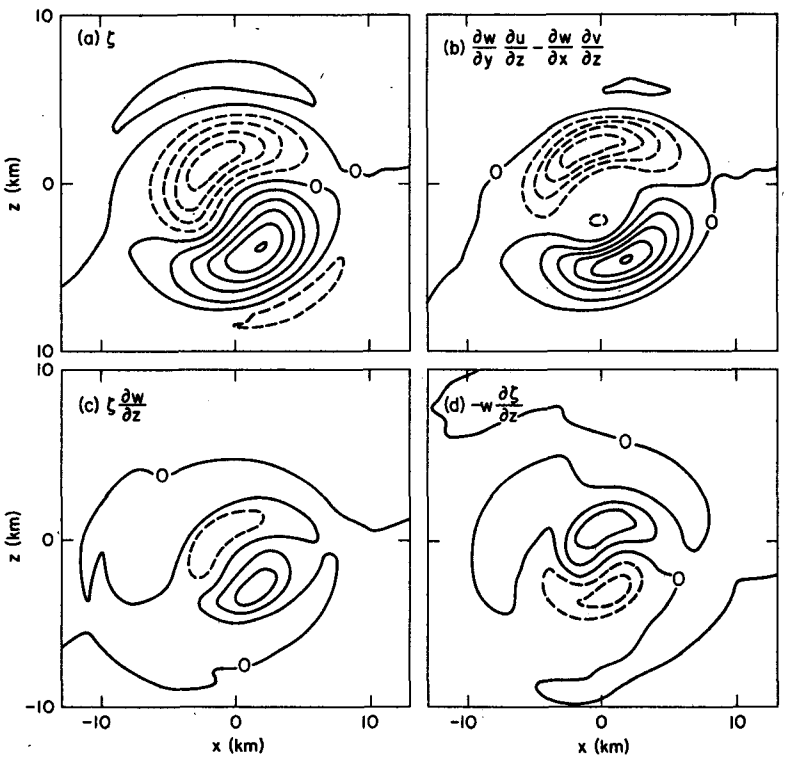

FIG. 10. Horizontal contour plots $z = 1.5$ km, $t = 10$ min for the curved hodograph case in Fig. 5 of (a) the vertical vorticity and the vorticity production terms in Eq. (20), *viz.*, (b) tilting, (c) stretching and (d) vertical advection. Vorticity is contoured in 0.008 s^{-1} increments while the production terms are contoured at 4×10^{-6} s^{-2} intervals.

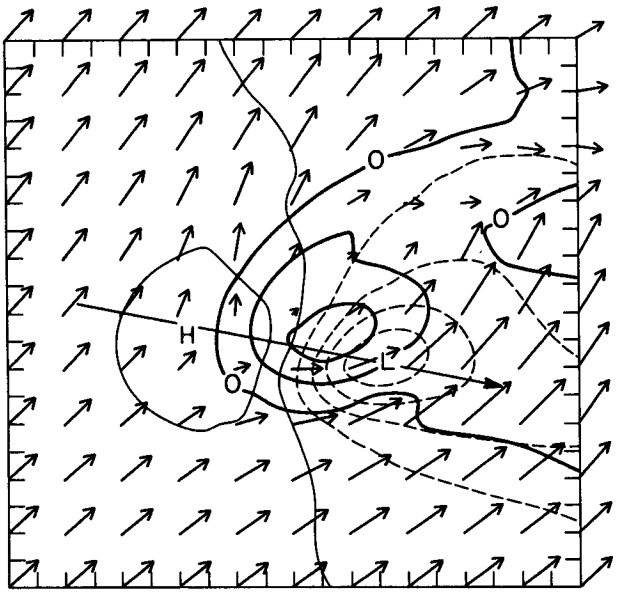

FIG. 11. Horizontal contour plot of vertical velocity (heavy solid lines, 10 m s^{-1} intervals), pressure (thin solid line, 0.5 mb intervals) and horizontal vector winds (10 m s^{-1} corresponds to a 1 km grid interval) at z = 6 km, t = 40 min from the three-dimensional numerical cloud model simulation of Fig. 2b. Long arrow represents direction of the environmental wind-shear vector at this level. Note that the pressure pattern aligns with the shear vector rather than the storm relative winds.

environmental shear. To understand why this bias should amplify the positive vorticity, consider the vertical vorticity equation obtained from the curl of (1):

$$\frac{\partial \zeta}{\partial t} = -\mathbf{v}\cdot\nabla\zeta + \mathbf{k}\cdot\left(\frac{\partial \mathbf{v}}{\partial z}\times\nabla w\right) + \zeta\frac{\partial w}{\partial z}. \quad (20)$$

That is, the vertical vorticity at a fixed location can change by advection, tilting horizontally oriented vorticity to or from the vertical direction and stretching of vortex tubes (cf. Dutton, 1976, pp. 339–343). Figs. 10a–10d contain horizontal contour plots of vorticity, tilting, stretching and vertical advection of ζ at t = 10 min, z = 1.5 km which correspond to w as shown in Fig. 6b. We note that tilting and stretching are both biased toward the right. It appears that the increased vertical velocity on the right flank of the original updraft acts to preferentially increase the horizontal gradient of w on that side and therefore increase the amount of vortex tilting preferentially on the right. Another contribution to the bias is the increased vertical velocity near the ground to the right of the shear vector which increases convergence of the positive vorticity, i.e., vortex stretching acts preferentially on the positive member of the vortex pair. Vertical advection is more or less symmetric and tends to oppose the stretching effect at this time. Horizontal advection is small and hence not displayed.

c. *Comments on the obstacle flow analogy*

It has been noted many times in the literature that the horizontal flow around severe thunderstorms at mid-levels resembles flow around an obstacle as observed in laboratory fluid dynamics experiments (cf. Newton, 1960). And indeed at certain levels it does resemble flow around a circular cylinder at high Reynolds number where separation occurs on the lee side. The value of such an observation is that which is known about the laboratory flow can be used to understand atmospheric flow. In the laboratory flow, there is high pressure at the forward stagnation point and low pressure in the rear due to flow separation. So, the analogy goes, in a frame of reference moving with the thunderstorm (cylinder), high pressure should be observed at the point where the relative winds divide (stagnation point) to go around the thunderstorm with low pressure in the wake. However, this analogy is complicated by the fact that significant amounts of air are flowing into or out of the storm over most of its depth, making it a rather porous cylinder. Furthermore, since the storm relative wind direction varies considerably with height, the three-dimensional aspects of the pressure distribution could be substantial. We believe the present analysis is preferable since it is derived from the relevant equations of motion without analogies to other flow systems. A major difference between our analysis and the obstacle flow analogy is that our result predicts that *the pressure gradient across the updraft is in the direction of the environmental wind-shear vector rather than the direction of the storm relative winds at a given height.* This result is illustrated in Fig. 11 which is taken from the full three-dimensional cloud model simulation displayed in Fig. 2b. Shown is the horizontal contour plot of vertical velocity and pressure together with the horizontal flow vectors and the environmental shear vector at z = 6.0 km, t = 40 min. Although the storm relative flow is toward the northeast, the high/low pressure pattern is more nearly aligned with the shear vector which points to the east-southeast and is consistent with Eq. (11). Similar alignments with the shear vector rather than the storm relative flow is apparent at an earlier time in Fig. 4. The prediction of Eq. (11) is independent of any *a priori* estimate of storm relative motion.

d. *Summary*

The primary objective of the present work is to explain how a veering environmental-shear vector can bias an initially symmetric updraft to grow to the right of the shear vector and acquire cyclonic rotation, even though there is initially no environmental rotation. The explanation offered is based on a linear theory where it is assumed amplitudes are small. To evaluate the extent to which the linear

theory can describe events in a situation where amplitudes are large, we integrated the three-dimensional, shallow, anelastic equations using a simple parameterization of the latent heating within a cloud and analyzed linear and nonlinear effects separately. We have found the results to depend strongly on the directional variations of the wind shear vector.

1) When the shear vector does not veer with height, the numerical integrations show than an initially symmetric updraft can split in two even though no rain process was included. We propose that the vortex pair produced by the upward tilting of (horizontal) environment vorticity, together with the horizontal vorticity produced by horizontal buoyancy gradient, creates low pressure on the updraft flanks at midlevels, thereby forcing vertical motion on the flanks. These are, essentially, nonlinear effects. Wilhelmson and Klemp (1978) attributed storm splitting to an accumulation of rainwater on the axis of the initial updraft. However, recomputing the cloud model simulation shown in Fig. 2a with rain processes turned off, splitting did occur, although it took much longer to develop and the split storms moved apart much more slowly. Consequently, although the rainwater loading effect may dominate the splitting process, the dynamic forcing may also play a significant role.

2) When the shear vector veers with height, the updraft splitting occurs as before but note the right member of the split pair is stronger and has stronger positive vertical vorticity than the left member has negative. Computation of the terms in the vertical momentum equation demonstrates that the linear effect is the only one which can account for this rightward bias. Further, the linear theory can also account for the increased positive vorticity on the right flank because the increase in $|\nabla w|$ on that flank implies an increased tilting of the environmental vorticity.

APPENDIX

Pressure Analysis

Eq. (14) is Poisson's equation which we write here as

$$\nabla^2\pi = f(\mathbf{x}, t). \tag{A1}$$

We require periodicity of the solution over the horizontal domain size. Since $w = 0$ at the upper and lower boundaries, the conditions on π at these boundaries (from Eq. 5) are

$$\left.\begin{aligned}\frac{\partial\pi}{\partial z}(x, y, 0, t) &= B(x, y, 0, t)\\ \frac{\partial\pi}{\partial z}(x, y, z_T, t) &= B(x, y, z_T, t)\end{aligned}\right\}. \tag{A2}$$

The initial condition for the integration presented in Section 3 [Eq. (19)] has zero buoyancy at $z = 0$ and z_T. Because there is no diffusion in this model, the buoyancy remains zero at the boundary for all time. Without loss of generality we consider the two-dimensional version ($\partial/\partial y = 0$, say) of Eqs. (A1) and (A2). The solution is

$$\pi(x, z, t) = L^{-1}\int_{-L/2}^{L/2} dx'\left[\int_0^z (z - z')f(x', z', t)dz'\right] + 2L^{-1}\sum_{n=1}^{\infty} k_n^{-1}\int_{-L/2}^{L/2} dx'\cos k_n(x - x')\left[\int_0^z f(x', z', t)\sinh k_n(z - z')dz' - \frac{\cosh k_n z}{\sinh k_n z_T}\int_0^{z_T} f(x', z', t)\cosh k_n(z_T - z')dz'\right], \tag{A3}$$

where L is the domain length and $k_n \equiv 2n\pi L^{-1}$.

The derivative of (A3) with respect to z is

$$\frac{\partial\pi}{\partial z} = L^{-1}\int_{-L/2}^{L/2} dx'\left[\int_0^z f(x', z', t)dz'\right] + 2L^{-1}\sum_{n=1}^{\infty}\int_{-L/2}^{L/2} dx'\cos k_n(x - x')\left[\int_0^z f(x', z', t)\cosh k_n(z - z')dz' - \frac{\sinh k_n z}{\sinh k_n z_T}\int_0^{z_T} f(x', z', t)\cosh k_n(z_T - z')dz'\right]. \tag{A4}$$

We analyze the contribution to π from the forcing function f which may be arbitrarily decomposed to isolate different physical effects. It is important to note $\pi(x, y, t) = P[f]$ where $P[f]$ is a *linear* functional of f. If we let $f = f_1 + f_2$, say, then $\pi_1(x, y, t) = P[f_1]$ and $\pi_2(x, y, t) = P[f_2]$ where π_1 and π_2 both independently satisfy Eqs. (A1)-(A2).

The analysis in Section 3 considers the contribution to the pressure from linear, nonlinear and buoyancy terms. Formally, we solve the three equations

$$\nabla^2\pi_L = -2\left(\frac{dU}{dz}\frac{\partial w}{\partial x} + \frac{dV}{dz}\frac{\partial w}{\partial y}\right), \tag{A5}$$

$$\nabla^2\pi_{NL} = -\left(\frac{\partial u}{\partial x}\right)^2 - \left(\frac{\partial v}{\partial y}\right)^2 - \left(\frac{\partial w}{\partial z}\right)^2$$

$$-2\frac{\partial u}{\partial z}\frac{\partial w}{\partial x}-2\frac{\partial v}{\partial z}\frac{\partial w}{\partial y}-2\frac{\partial u}{\partial y}\frac{\partial v}{\partial x}, \quad \text{(A6)}$$

$$\nabla^2\pi_B=\frac{\partial B}{\partial z}, \quad \text{(A7)}$$

where the solutions for π_L, π_{NL} and π_B are each required to be horizontally periodic. Evaluating (A4) at $z = 0$ and z_T for the forcing functions in (A5)–(A7) confirms that

$$\left.\begin{aligned}\frac{\partial\pi_\alpha}{\partial z}(x, y, 0, t)=0\\ \frac{\partial\pi_\alpha}{\partial z}(x, y, z_T, t)=0\end{aligned}\right\}, \quad \text{(A8)}$$

where α is L, NL or B. Since the lateral boundary conditions are periodic, Eqs. (A5)–(A7) are solved by first taking the fast Fourier transform in the x and y directions, then solving the resulting ordinary differential equation in z by inversion of a tri-diagonal matrix.

REFERENCES

Brooks, E. M., 1949: The tornado cyclone. *Weatherwise*, **2**, 32–33.

Browning, K. A., 1964: Airflow and precipitation trajectories within severe local storms which travel to the right of the winds. *J. Atmos. Sci.*, **21**, 634–639.

——, 1968: The organization of severe local storms. *Weather*, **23**, 429–434.

Dutton, J. A., 1976: *The Ceaseless Wind*. McGraw Hill, 579 pp.

Fujita, T. T., 1960: Mother cloud of the Fargo tornadoes of 20 June, 1957. *Cumulus Dynamics*, Pergamon Press, 211 pp. (see pp. 175–177).

Klemp, J. B., and R. B. Wilhelmson, 1978a: The simulation of three-dimensional convective storm dynamics. *J. Atmos. Sci.*, **35**, 1070–1096.

——, and ——, 1978b: Simulations of right- and left-moving storms produced through storm splitting. *J. Atmos. Sci.*, **35**, 1097–1110.

——, —— and P. S. Ray, 1981: Observed and numerically simulated structure of a mature supercell thunderstorm. *J. Atmos. Sci.*, **38**, 1558–1580.

Lilly, D. K., 1960: On the theory of disturbances in a conditionally unstable atmosphere. *Mon. Wea. Rev.*, **88**, 1–17.

Maddox, R. A., 1976: An evaluation of tornado proximity wind and stability data. *Mon. Wea. Rev.*, **104**, 133–142.

Marwitz, J. D., 1972: The structure of severe hailstorms. Part III: Severely sheared storms. *J. Appl. Meteor.*, **11**, 189–201.

Newton, C. W., 1960: Hydrodynamic interactions with ambient wind field as a factor in cumulus development. *Cumulus Dynamics*, Pergamon Press, 211 pp. (see pp. 135–144).

Newton, C. W., and H. R. Newton, 1959: Dynamical interactions between large convective clouds and environment with vertical shear. *J. Meteor.*, **16**, 483–496.

Ogura, Y., and N. A. Phillips, 1962: Scale analysis of deep and shallow convection. *J. Atmos. Sci.*, **19**, 173–179.

Prandtl, L., and O. G. Tietjens, 1934: *Fundamentals of Hydro- and Aeromechanics*. Dover, 270 pp.

Schlesinger, R. E., 1978: A three-dimensional numerical model of an isolated thunderstorm: Part I. Comparative experiments for variable ambient wind shear. *J. Atmos. Sci.*, **35**, 690–713.

——, 1980: A three-dimensional numerical model of an isolated thunderstorm. Part II: Dynamics of updraft splitting and mesovortex couplet evoluation. *J. Atmos. Sci.*, **37**, 395–420.

Wilhelmson, R. B., and J. B. Klemp, 1978: A numerical study of storm splitting that leads to long-lived storms. *J. Atmos. Sci.*, **35**, 1974–1986.